Wave generation and energetic electron scattering in solar flares

HANQING MA,[1] J. F. DRAKE,[1] AND M. SWISDAK[2]

[1]*Department of Physics, University of Maryland, College Park, MD 20740, USA*
[2]*IREAP, University of Maryland, College Park, MD 20742, USA*

ABSTRACT

We conduct two-dimensional particle-in-cell simulations to investigate the scattering of electron heat flux by self-generated oblique electromagnetic waves. The heat flux is modeled as a bi-kappa distribution with a $T_\parallel > T_\perp$ temperature anisotropy maintained by continuous injection at the boundaries. The anisotropic distribution excites oblique whistler waves and filamentary-like Weibel instabilities. Electron velocity distributions taken after the system has reached a steady state show that these instabilities inhibit the heat flux and drive the total distributions towards isotropy. Electron trajectories in velocity space show a circular-like diffusion along constant energy surfaces in the wave frame. The key parameter controlling the scattering rate is the drift speed of the heat flux v_d compared with the electron Alfvén speed v_{Ae}, with higher drift speeds producing stronger fluctuations and a more significant reduction of the heat flux. Reducing the density of the electrons carrying the heat flux by 50% does not significantly affect the scattering rate. A scaling law for the electron scattering rate versus v_d/v_{Ae} is deduced from the simulations. The implications of these results for understanding energetic electron transport during solar flare energy release are discussed.

Keywords: Active solar corona (1988), Plasma physics (2089), Solar flares (1496), Solar coronal waves (1995)

1. INTRODUCTION

In solar flares electrons can be accelerated to energies above 100 keV (Lin et al. 2003; Krucker et al. 2007, 2010b), three orders of magnitude higher than typical ambient coronal values. Because the X-rays and microwaves produced by solar energetic electrons are observed in both the corona (the location of the initial energization) and the chromosphere, transport, a crucial process that remains poorly understood, must be a key component of the dynamics of flare energy release. Observations point to a mechanism (or mechanisms) that scatter and inhibit electron transport (Simões & Kontar 2013; Fleishman et al. 2022). Transport effects can also modify the energy distribution of the propagating electrons and the observed X-ray spectra, which complicates the identification of acceleration mechanisms.

Magnetic reconnection is thought to control the release rate of magnetic energy in flares (Yamada et al. 2010; Hesse & Cassak 2020), occurring on lengthscales reaching 10^4 km over timescales on the order of tens of seconds. Thus, in the absence of scattering, a relativistic electron will take less than 0.1s to escape from a flare region. However, observations of above-the looptop sources reveal that the lifetime of energetic electrons is two orders of magnitude longer than the free-streaming transit time (Masuda et al. 1994; Krucker et al. 2007, 2010b; Fleishman et al. 2022), which suggests suppression of the transport of energetic electrons.

Observations have revealed the existence of looptop hard X-ray sources during flares (Masuda et al. 1994; Krucker et al. 2008; Guo et al. 2012; Simões & Kontar 2013; Fleishman et al. 2022). These sources are situated at or distinctly above the top of the soft X-ray flaring loops. Increased detection sensitivity indicates that the above-the-looptop hard X-ray emission is likely a common feature of all flares (Petrosian et al. 2002). Such sources require that the transport of energetic electrons be inhibited in the acceleration region so that bremsstrahlung can produce the fluxes of hard X-rays. Further, it has been shown that the fluxes of energetic electrons in the looptop are several times (a factor of $1.7 - 8$) higher than the fluxes of electrons reaching the footpoints during the flare impulsive phase (Simões & Kontar 2013), suggesting an accumulation of electrons in the looptop. Thus, Simões & Kontar (2013) con-

cluded that accelerated electrons must be subjected to a trapping mechanism that holds a significant fraction of them inside the coronal loops.

A long-standing issue in solar physics (Moore et al. 1980) is that the observed cooling times of soft X-ray sources are much longer than the predictions from models where cooling proceeds by collision-dominated (Spitzer 2006) conduction. This finding gives a powerful motivation to consider the possible limitation of heat conduction by a confinement mechanism that inhibits the transport of energetic electrons. The turbulent suppression of heat conduction is one possibility. Turbulent fluctuations in the ambient magnetic field act to enhance the angular scattering rate and thus reduce the rate of escape of energetic electrons from the acceleration region (Bian et al. 2018). But, numerical results show that to account for the observations the turbulence generated by the energy release should persist beyond the impulsive phase, which requires an extended release of magnetic energy (Bian et al. 2018).

The above theoretical and observational evidence has led people to consider potential mechanisms that can scatter and confine energetic electrons in the corona. One possible mechanism is the formation of a highly localized electrostatic potential drop, in the form of a double layer (DL), that inhibits the transport of energetic electrons (Li et al. 2012, 2013, 2014). However, Li et al. (2013, 2014) found that the effectiveness of confinement by a DL is proportional to the magnitude of the DL potential drop, which scales as T_{eh}, the hot electron temperature. Since $T_{eh} \ll m_e c^2$, the strength of the DL is not sufficient to inhibit the transport of nonthermal electrons. Another possibility is magnetic trapping, for which an effective mirror requires significant perpendicular electron velocities. The observations of strong microwave-producing gyrosynchrotron emission, which arises mainly from a trapped population of electrons spiraling in coronal magnetic loops, also requires significant perpendicular electron energy (Gary et al. 2018). However, recent studies of reconnection (Drake et al. 2006; Dahlin et al. 2014, 2016) suggested that the primary energy gain during the acceleration process is parallel to the ambient magnetic field. Therefore, to account for the observations and facilitate magnetic trapping, a mechanism must develop to scatter the energetic electron parallel motion into the perpendicular direction.

A potential mechanism is scattering by oblique whistler waves (Roberg-Clark et al. 2016, 2018a,b, 2019). The cold plasma dispersion relation of a whistler wave is

$$\omega = \frac{|k_\parallel| k d_e^2 \Omega_e}{1 + k^2 d_e^2} \qquad \text{or} \qquad \frac{v_\parallel}{v_{Ae}} = \frac{k d_e}{1 + k^2 d_e^2} \tag{1}$$

where ω is the wave frequency, $k_\parallel$ is the wave number along the direction of the uniform background magnetic field B_0, v_{Ae} is the electron Alfvén speed and d_e is the electron skin depth. The parallel phase speed $v_\parallel$ first increases then decreases with $k d_e$, with a maximum of $0.5 v_{Ae}$ when $k d_e = 1$. Thus, the characteristic phase speed of whistler waves is $\sim v_{Ae}$. According to the quasilinear theory of whistler wave scattering (Stix 1992), resonant particles diffuse in velocity space along curves of constant energy in the wave frame (i.e., the reference frame that moves with the wave parallel phase speed $v_{ph} = \omega/k_\parallel$ along B_0). Thus, the diffusive flux of particles is locally tangent to semicircles centered on the parallel phase velocity v_{ph} of whistler waves given by

$$\left(v_\parallel - v_{ph}\right)^2 + v_\perp^2 = constant \tag{2}$$

For diffusion along this path, the particle's energy is conserved in the whistler wave frame, but not conserved in the lab frame, where the particle's kinetic energy is transferred to the wave's growth. Waves and particles can participate in resonant wave–particle interactions when they fulfill the resonance condition

$$\omega - k_\parallel v_\parallel - n\Omega_e = 0 \tag{3}$$

where $\Omega_e = eB_0/m_e c$ is the electron cyclotron frequency, n is an integer that can take on positive and negative values (Krall & Trivelpiece 1973), and B_0 is the guiding field strength. $n = 0$ gives the Landau resonance condition while $n = 1, -1$ correspond to the normal and anomalous cyclotron resonances, respectively.

Significant scattering at resonant velocities can lead to the appearance of "horn-like" structures in the electron distribution function (Roberg-Clark et al. 2019; Vo 2021) in which the tail exhibits circular bumps at each resonant velocity. Verscharen et al. (2019) show that the necessary condition to have wave growth is $0 < v_{ph} < U_{0s}$, with U_{0s} the heat flux average bulk velocity. Only in this way can the resonant particles lose kinetic energy as they diffuse and transfer energy to the growing resonant wave. Furthermore, as the wave amplitude increases, the resonance widths get larger and can eventually overlap (Karimabadi et al. 1992; Roberg-Clark et al. 2016; Vo et al. 2022). The particle

motion before the resonances overlap is periodic, but after the overlap it becomes diffusive. As a result, particles starting at small pitch-angles can scatter past 90 degrees if the wave amplitude is above the overlap threshold.

Heat flux suppression by oblique whistler waves in the fast solar wind is under active study (Verscharen et al. 2019; Vasko et al. 2019; López et al. 2019; Micera et al. 2020). In the solar wind, the heat flux is carried by the strahl, which appears as a field-aligned beam in the electron distribution. Observations reveal evidence that the strahl is scattered into the halo (Maksimovic et al. 2005; Graham et al. 2017; Štverák et al. 2009), the superthermal component of the solar wind. Particle-in-cell simulations (López et al. 2019; Micera et al. 2020) and quasi-linear analysis (Vasko et al. 2019) have shown that for typical parameters the strahl electrons are capable of generating oblique whistler waves via the first anomalous cyclotron resonance (see equation 3), which is known as the fan instability or the instability of runaway electrons (Kadomtsev & Pogutse 1968; Parail & Pogutse 1978). The oblique whistler waves were shown to be able to drive pitch-angle scattering of the strahl, suppressing the heat flux and resulting in formation of the halo. Thus, the observations of the scattering of the strahl by whistler waves suggest that reconnection-driven energetic electrons should also drive and be scattered by oblique whistler waves.

Another possibility is the Weibel (also known as the filamentation) instability (Weibel 1959), which is driven by an electron thermal anisotropy and can self-generate transverse magnetic perturbations with wave vectors perpendicular to the direction of the higher temperature. In the reconnection context the instability is driven when $T_\parallel \gg T_\perp$, the wavevector $\mathbf{k}$ is perpendicular to the ambient magnetic field and the magnetic field perturbation is perpendicular to both $\mathbf{k}$ and the local magnetic field. The signature of this instability is a pattern of current filaments and transverse magnetic fields stretched along the ambient field. The Weibel instability has been intensively studied theoretically (Yoon & Davidson 1987; Yoon 2007), numerically (Morse & Nielson 1971; Fonseca et al. 2003), and experimentally (Allen et al. 2012; Huntington et al. 2015) and has been considered a possible mechanism for heat transfer inhibition and thermal conduction limitation in laser-plasma experiments (Weihan & Min 1985; Levinson & Eichler 1992). In this study, under sufficiently strong heat flux conditions, the temperature anisotropy within the kappa distribution can trigger the Weibel instability. The competition between whistler and Weibel instabilities is complicated, and the Weibel instability is typically found to be transient, eventually giving way to the development of whistler waves once the temperature anisotropy has been reduced.

In previous simulations treating high-β systems (Komarov et al. 2018; Roberg-Clark et al. 2018a,b) a temperature gradient was imposed across the system to drive the heat flux so that the resulting whistler waves could be evolved to steady state. In later simulations with $\beta \sim 1$ oblique whistlers were driven by an initial anisotropic kappa distribution function so the waves grew to large amplitude but then decayed due to the fast relaxation of the initial anisotropy (Roberg-Clark et al. 2019). In this study, we consider a system in which the heat flux arises from electrons with a bi-kappa distribution propagating parallel to the ambient magnetic field. In order to drive the system to a steady state, electrons reaching the boundaries are injected on the opposite ends of the computational domain with new velocities that ensure a continual input of heat flux. Oblique whistlers are initially excited by the anisotropic distribution through the $n = -1$ anomalous cyclotron resonance. Weibel perturbations are also evident early in the simulations. At later times, the influence of the initial distribution decays and the heat flux injection from the boundary sources continues to drive the oblique whistlers. The waves resonate with and scatter the most energetic electrons through overlapping resonances, reducing the skewness of the total distribution function and limiting the heat flux.

2. SIMULATION METHOD

We carry out 2D simulations (in the $x - y$ plane) using the PIC code p3d (Zeiler et al. 2002), which calculates particle trajectories using the relativistic Newton—Lorentz equations and advances the electromagnetic fields using Maxwell's equations. There is an initial uniform magnetic field $\mathbf{B} = B_0\hat{\mathbf{y}}$ threading the plasma, so that v_y is the initial parallel velocity and v_x and v_z are the initial perpendicular velocities. The initial electron distribution function has two components. The first is a bi-kappa distribution with a heat flux in the positive v_y direction:

$$f_\kappa\left(v_\parallel, v_\perp\right) = \frac{n_0}{(\pi\kappa)^{3/2}\theta_\parallel\theta_\perp^2}\frac{\Gamma\left(\kappa+1\right)}{\Gamma\left(\kappa-\frac{1}{2}\right)}\left[1 + \frac{v_\parallel^2}{\kappa\theta_\parallel^2} + \frac{v_\perp^2}{\kappa\theta_\perp^2}\right]^{-(\kappa+1)}\Theta\left(v_\parallel\right) \tag{4}$$

where n_0 is the electron density, Γ is the gamma function, κ is a parameter that tunes the steepness of the nonthermal tail of the distribution, and

$$\theta_n^2 = v_{th,n}^2\left(\kappa - 3/2\right)/\kappa \tag{5}$$

is the effective thermal speed, $v_{th,n}^2 = 2T_n/m_e$ is the regular thermal speed, where T_n is the temperature in the n-direction, m_e is the electron mass and $\Theta\left(v_\parallel\right)$ is the Heaviside step function.

The second component is a drifting Maxwellian distribution that represents the cold return current beam (moving against B_0)

$$f_M\left(v_\parallel, v_\perp\right) = \frac{n_0}{\pi^{3/2} v_T^3 \left[1 + \text{erf}(v_d/v_c)\right]} \exp\left\{-\left[\left(v_\parallel + v_d\right)^2 + v_\perp^2\right]/v_c^2\right\}\Theta\left(-v_\parallel\right) \tag{6}$$

where $v_c^2 = 2T_c/m_e$ is the cold thermal speed, v_d is a drift speed that ensures initial zero current, while the error function $\text{erf}(v_d/v_c)$ makes the density of hot and cold particles equal. This distribution choice is motivated by flare observations (Krucker et al. 2010a; Oka et al. 2013; Warmuth & Mann 2016; Aschwanden et al. 2017; Glesener et al. 2020) that suggest a power-law distribution of nonthermal electrons in the energy-release and electron acceleration region.

For parameters, we chose $\kappa = 4$, $T_y = 20T_c = 40T_x$, $v_{th,y}/v_{Ae} = \sqrt{2}$, $c/v_{Ae} = 5$, $\beta_y = 8\pi n_0 T_y/B_0^2 = 2$. While this is a relatively high β for the corona, specific flare observations show a hard X-ray source β of approximately 1 (Krucker et al. 2010a). Recent simulation results also demonstrate that magnetic reconnection can drive the outflow to a marginal firehose state in which $\beta_\parallel - \beta_\perp \approx 2$ (Arnold et al. 2021). When the high energy tail of an anisotropic kappa distribution with $\kappa = 4$ is scattered to an isotropic one, particle number conservation implies the resulting energy spectral index will be 4.5 because the isotropic distribution occupies a larger phase space ($E^{0.5}$) than the anisotropic one ($E^{-0.5}$). This value is consistent with the results of a statistical study of flare parameters, which found that the spectral index value is around 4 based on a single power law fit (Warmuth & Mann 2016). Additionally, the large value of $T_\parallel/T_\perp$ is motivated by 3D PIC simulations of reconnection showing $P_\parallel/P_\perp$ approximately equal to 100 (Dahlin et al. 2017).

To determine the nonthermal β, we separate the kappa distribution into a combination of a Maxwellian component and a nonthermal component, where the temperature of the Maxwellian component (T_M) is related to the kappa distribution temperature (T_κ) by the equation $T_M = (\kappa - 1.5)T_\kappa/\kappa$ (Oka et al. 2013). Oka et al. (2013) define the number density of the Maxwellian component (N_M) by requiring it to match the differential flux of the kappa distribution at energy T_M. The result is

$$N_M = n_0 \exp\left(1\right)\left(\frac{1}{\kappa}\right)^{\frac{3}{2}}\frac{\Gamma\left(\kappa+1\right)}{\Gamma\left(\kappa-\frac{1}{2}\right)}\left[1+\frac{1}{\kappa}\right]^{-(\kappa+1)} \tag{7}$$

The density of the nonthermal component for the parameters under consideration can be calculated as $N_{NT} \approx 0.2n_0$. The nonthermal energy density is calculated with the energy relation $n_0 T_\kappa = N_M T_M + N_{NT} T_{NT}$ with $T_\kappa \approx T_\parallel/3$. The resulting nonthermal beta is 0.17, which is slightly larger than the observed value of around 0.1 near the flare looptop (Fleishman et al. 2020), but quite close to the 0.16 of another observation (Emslie et al. 2004).

The simulation domain lengths are $L_y = 163.84\,d_e$ and $L_x = L_y/4$, where $d_e = c/\omega_{pe}$ is the electron skin depth, and $\omega_{pe} = \left(4\pi n_0 e^2/m_e\right)^{1/2}$ is the electron plasma frequency. The simulation time step is $dt = 0.008\Omega_e^{-1}$, where $\Omega_e = eB_0/m_ec$ is the electron cyclotron frequency. Ions are initialized with a Maxwellian distribution of temperature $T_i = T_c$, and do not play an important role due to the large mass ratio $m_i/m_e = 1600$. The simulation uses 560 particles per species per cell and has a grid of 1024 by 4096 cells.

We set a boundary source to continuously inject heat flux into the system in order to drive the system to a steady state. Due to the initial distribution function (the total of equations (4) and (6)), the heat flux moves upwards in the box while a cold return current moves downwards. Electrons that encounter the top boundary are reinjected at the bottom of the box with random positions and new velocities that satisfy the kappa flux distribution

$$f_{\kappa f}\left(v_\parallel, v_\perp\right) = \frac{2\left(\kappa-1\right)}{\pi\kappa\left(\theta_\parallel \theta_\perp\right)^2}v_\parallel\left[1+\frac{v_\parallel^2}{\kappa\theta_\parallel^2}+\frac{v_\perp^2}{\kappa\theta_\perp^2}\right]^{-(\kappa+1)}\Theta\left(v_\parallel\right) \tag{8}$$

where θ_n^2 and other parameters are the same as the initial kappa distribution, Eq. (4). The kappa flux distribution models particles escaping from a source. Similarly, when electrons hit the bottom boundary, they are re-injected at the top of the box with random positions and new velocities that satisfy the drift Maxwellian distribution with identical parameters as in the initial distribution. The boundary condition in the x direction is periodic and ions, which are essentially only a charge-neutralizing background, simply follow periodic boundary conditions in all directions. The

electromagnetic boundary conditions are set to be periodic in both the parallel and perpendicular directions. The ratio v_d/v_{Ae}, where v_d is the mean parallel drift speed of the heat flux (see equations 4 and 8), is expected to be a key parameter controlling the degree to which the electron distribution is in resonance with the excited waves. In the simulations presented here we vary this parameter by changing the density n_0.
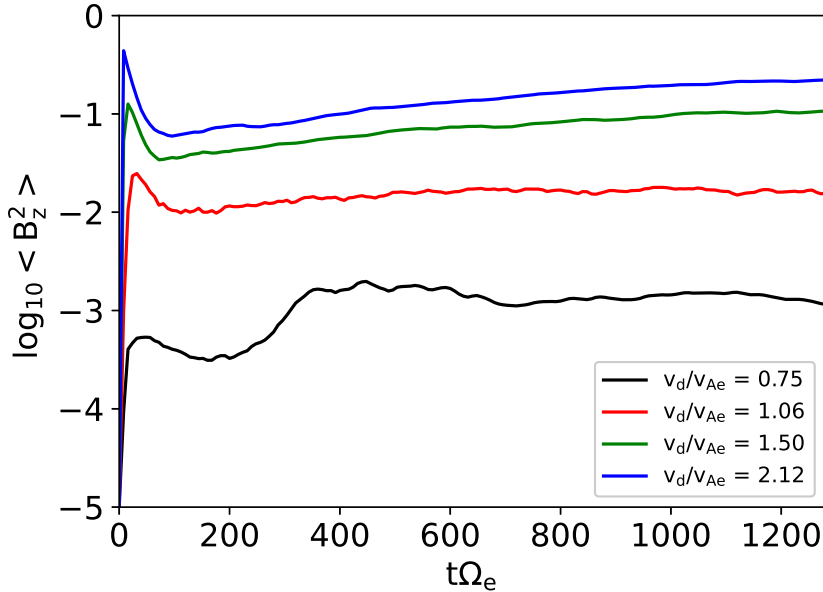
3. SIMULATION RESULTS

Figure 1. The evolution of the box-averaged out-of-plane magnetic field fluctuations for different cases of v_d/v_{Ae}, where v_d is the mean parallel drift speed of the heat flux and v_{Ae} is the electron Alfvén speed.

The initial distribution drives magnetic fluctuations unstable in the system. Figure 1 shows the box-averaged magnetic field fluctuation $\langle B_z^2 \rangle$ versus time for different values of v_d/v_{Ae}, where v_d is the mean parallel drift speed of the heat flux (Eq. (4)). The magnetic fluctuations grow rapidly, reach a peak value and, after a short decay, again grow slowly until flattening to a steady state at late time. The magnetic fluctuations reach larger amplitude for higher drift speeds, where more electrons have a velocity greater than the whistler phase speed and are therefore able to drive the waves.

Figure 2 shows the temperature anisotropy averaged over x versus distance y at the end of the simulations for different drift speeds. The higher drift speed cases (red, green and blue curves) exhibit roughly the same anisotropy at $y = 0$ as the systems have lost all information regarding the $t = 0$ initial conditions, while the slower drift speed case (black curve) is still affected by the initial distribution due to the weakness of the scattering. As a result, the anisotropy remains large. For higher drift speeds (green and blue curves), the temperature anisotropy decreases quickly with distance from the boundary and reaches a minimum value around 1.5. The final distribution is more isotropic at larger value of y because the injected electrons must propagate some distance into the domain before the waves are able to isotropize them. For the slower drift speed case (black curve), the anisotropy remains large due to the small amplitude of the waves, resulting in a correspondingly weak level of scattering.

Shown in Figure 3 is the ratio of the final to initial average y-directed heat flux for different drift speeds. The red point corresponds to a case where 25% of electrons, rather than 50%, initially satisfy the kappa distribution (Eq. (4)), while the remaining 75% are from the drifting Maxwellian distribution (Eq. 6)). In this case, all other distribution function parameters remain unaltered, with the exception of a reduction in the drift speed (see Eq. 6) that is necessary for current balance. In this case the density of nonthermal electrons carrying the heat flux is significantly reduced (Oka et al. 2013; Simões & Kontar 2013; Warmuth & Mann 2016). The heat flux at steady state decreases with increasing drift speed, reaching a minimum value around 40% of the initial heat flux for the highest drift speed. Notably, the reduced kappa density case (red point) does not significantly impact the reduction of the heat flux.
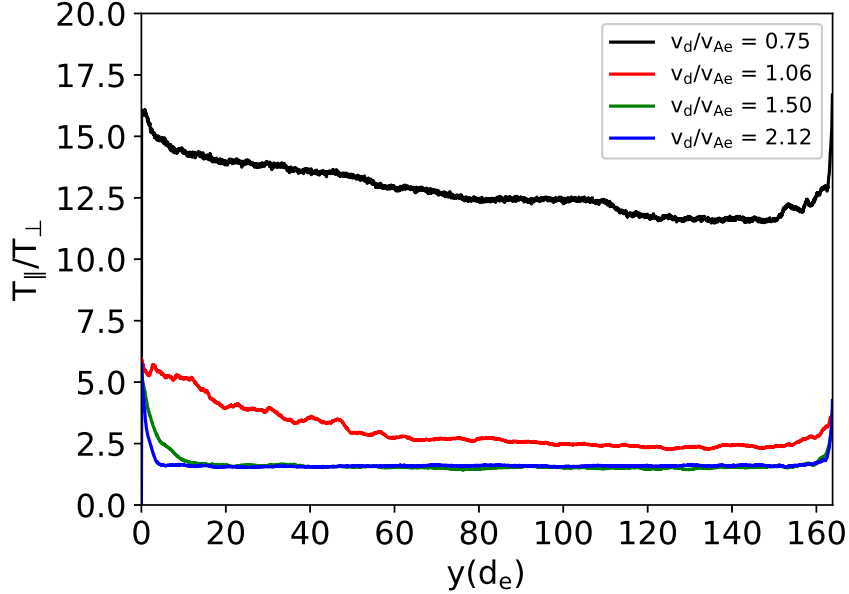
Figure 2. Ratio of the parallel electron temperature T_{eyy} to the perpendicular temperature $(T_{exx} + T_{ezz})/2$ of the total distribution at the end of the simulation for different values of v_d/v_{Ae}, where v_d is the mean parallel drift speed of the heat flux and v_{Ae} is the electron Alfvén speed.
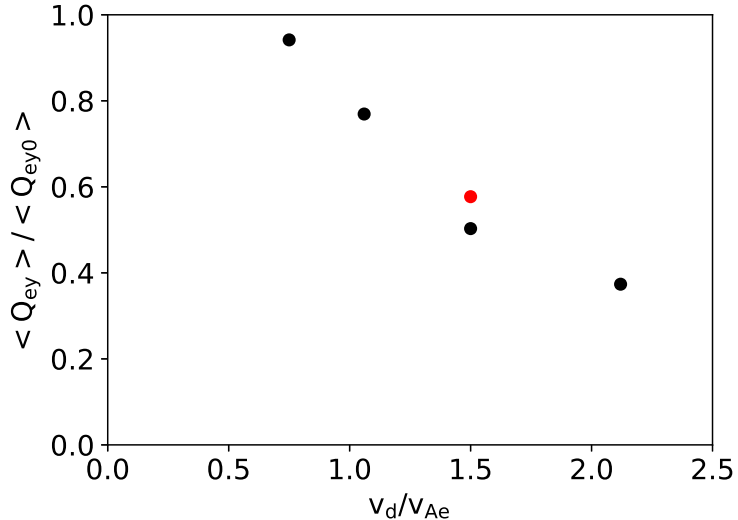

Figure 3. Ratio of final to initial y-directed average heat flux for different values of v_d/v_{Ae}, where v_d is the mean parallel drift speed of the heat flux and v_{Ae} is the electron Alfvén speed. The red point corresponds to a case in which 25% of electrons, rather than 50%, are found in the kappa distribution (Eq. (4)) at $t = 0$, while the remaining 75% are in the drifting Maxwellian distribution (Eq. (6)).

We now address the nature of the instabilities that drive electron scattering and specifically show that a strong Weibel instability develops in the high heat flux cases while whistlers dominate scattering at lower drift speeds. In Figure 4 we show the structure of the out-of-plane magnetic fluctuations and corresponding space-time plot for $v_d/v_{Ae} = 1.06$. Shown in Fig. 4(a) is the growth phase when the large anisotropy of the initial distribution excites the Weibel and produces filaments that fill the box along the heat flux direction. The spacing of these filaments along the y direction is around d_e. The magnetic structure of these filaments, with the wavevector **k** transverse to **B** and the magnetic perturbation dominantly in the z direction, matches the expected structure of a Weibel instability that is driven by the strong parallel heat flux. Such Weibel-like structures are soon replaced by larger-amplitude oblique whistler waves
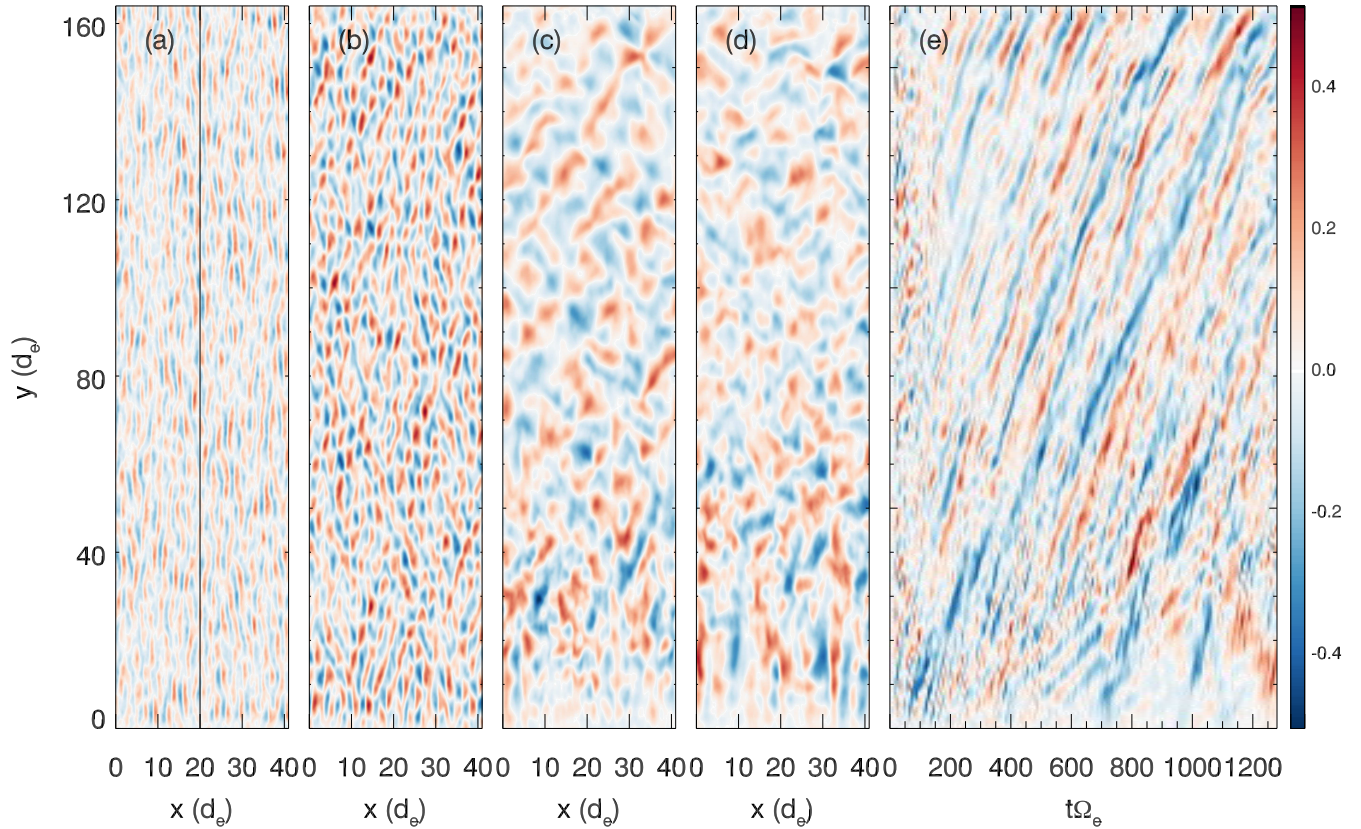
Figure 4. For the case with $v_d/v_{Ae} = 1.06$ two dimensional plots of the out-of-plane magnetic field B_z at (a) $t\Omega_e = 15$, (b) $t\Omega_e = 30$, (c) $t\Omega_e = 500$. and (d) $t\Omega_e = 1200$. Shown in (e) is the space-time diagram $(t - y)$ of B_z. The black line in (a) is where the space-time plot data shown in panel (e) is taken.

that propagate at angles of roughly $70°$ from the parallel direction, as shown in Figure 4(b). The whistlers are excited by the fan instability, which is driven by the $n = -1$ anomalous cyclotron resonance (see Eq. (3)) with the tail of the electron distribution. Figure 4(b) corresponds in time to the initial peak in the wave amplitude in Figure 1, so the initial peak and subsequent decay phase of the fluctuations should be associated with the drive from the initial distribution function. Figure 4(c) is at the time when the red curve in Figure 1 begins to flatten. Oblique whistler waves with normal angles around $45°$ are excited at the bottom of the box by heat flux injection and propagate upward. Filaments oriented along the y direction, which are excited by the Weibel instability, are also observed near the lower boundary; however, they occupy only a limited region near the lower boundary of the simulation domain. Figure 4(d) is taken at the end of the simulation and appears similar to panel (c), showing that the system has reached a steady state.

Shown in Fig. 4(e) is a space-time plot of B_z, where the data are collected from a strip extending over the entire y range of the domain at a fixed x position (vertical black line in Figure 4(a)). The initial peak-and-decay phase of the magnetic field fluctuation appears as a transient period before $t\Omega_e = 100$, after which upward-moving whistler waves appear throughout the entire box. After around $t\Omega_e = 100$, the bottom boundary continuously generates upward-moving whistler waves, showing that the instability from heat flux injection is responsible for the fluctuations at late time. The phase speed of the whistlers over most of the domain remains nearly constant during the entire simulation following the transient Weibel instability phase at very early time.

Figure 5 shows the power spectrum of the out-of-plane magnetic field for the simulation shown in Fig. 4. Figure 5(a) corresponds to the oblique whistler waves induced by the initial distribution (see Fig. 4(b)), exhibits peaks around $k_x d_e \sim 1.5$ and $k_y d_e \sim 0.6$, and shows power extending over a broad range of wave numbers. The wave normal angle for the highest-amplitude mode is around $70°$, but the range of wave numbers indicates the coexistence of several oblique waves with slightly different phase speeds. The parallel phase speed $\sim 0.5 V_{Ae}$ measured in Figure 4(b) corresponds
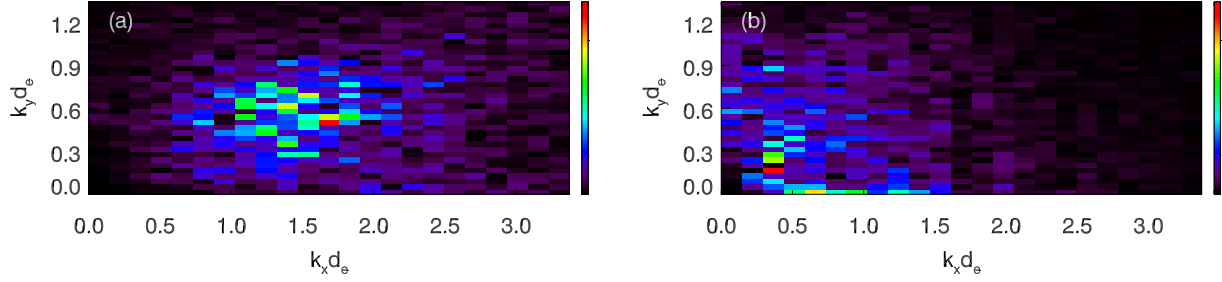
Figure 5. Power spectrum of the out-of-plane magnetic field B_z from the simulation in Figure 4 at: (a) $t\Omega_e = 30$ (see Fig. 4(b)); and (b) $t\Omega_e = 1200$ (see Fig. 4(d)).

to $kd_e \sim 1$ from the dispersion relation of Eq. (1), a value consistent with the power spectrum in Fig. 5(a). In the steady state, there are two peaks in the power spectrum, as shown in Figure 5(b). One is the oblique mode centered around $k_x d_e \sim 0.3$ and $k_y d_e \sim 0.2$, which corresponds to the oblique whistler wave. The other is a perpendicular mode centered around $k_x d_e \sim 0.6$ and $k_y d_e = 0$, which arises from the filaments appearing near the bottom boundary of Figure 4(d). The parallel phase speed $\sim 0.2 V_{Ae}$ measured at the end of the simulation gives $kd_e \sim 0.1$ from the dispersion relation of Eq. (1), which is consistent with Figure 5(b).
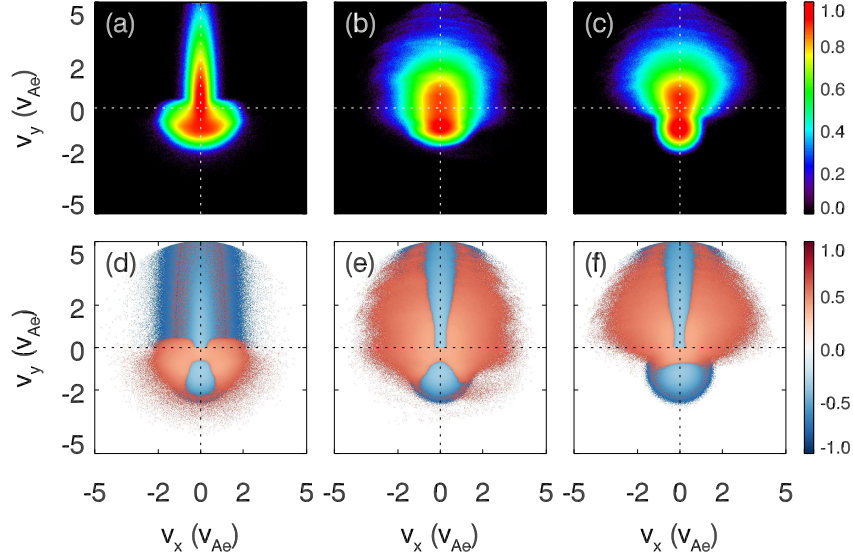

Figure 6. Electron distribution functions in $v_x - v_y$ phase space at the end of the simulation of Figure 4 at different y positions in the box. The sampling area of each position is the entire x range and 1% of the total y range. Shown in panels (a-c) are the electron velocity distribution functions on a logarithmic scale near the bottom, middle and top of the box, corresponding to positions at 0%, 80% and 99% of the total y range, respectively. Panels (d-f) are comparisons to the initial distribution, $\log\left(|f_{end} - f_{ini}|\right) \text{sgn}\left(f_{end} - f_{ini}\right)$, at the same positions, where sgn is the sign function.

The electron velocity-space distribution functions of Fig. 6 demonstrate the impact of the scattering of electrons by the wave activity. Shown in panels (a-c) are distributions from the end of simulation at different positions in the box. Figure 6(a), from the bottom of the simulation domain, is a kappa-like distribution in the upper half of the panel because of heat flux injection at the bottom boundary. The return current in the negative v_y plane is broadened in the v_x direction, due to scattering by whistler waves through the cyclotron resonance. In the upper half of the box, shown in Fig. 6(b), the total distribution has become nearly isotropic. The upward moving electrons have been strongly scattered. There is no obvious horn-like structure, which is likely a consequence of the overlap of several resonance circles (Vo et al. 2022) and is implied by the broad range of wave numbers shown in Figure 5. At the top of the box, panel (c), the cold current injection from the top boundary produces a beam feature in the negative v_y component,

while the positive v_y distribution is even more isotropic than in panel (b). Panels (d-f) show the difference between the final and initial distributions at the respective positions. Panel (d) shows that the return current has been heated, and in panels (e,f) the decrease in the parallel heat flux and the significant increase in the perpendicular velocity are direct evidence of the scattering of the nonthermal electrons by whistler waves.
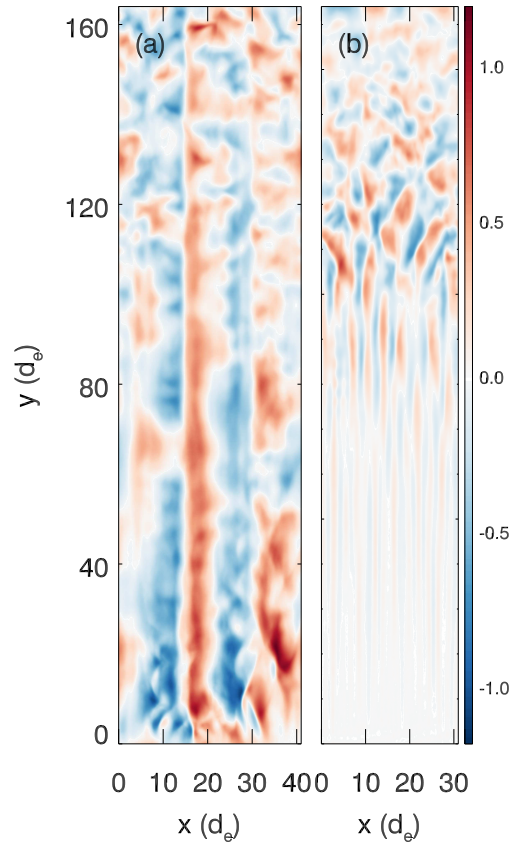

Figure 7. Two dimensional plots of the out-of-plane magnetic field B_z at $t\Omega_e = 1280$. In (a) the normal setup with $v_d/v_{Ae} = 1.50$ (as shown in Figs. 1 and 2) and in (b) the case with the reduced number density carrying the heat flux.

Shown in Fig. 7 is the structure of the out-of-plane magnetic fluctuations at the end of the simulations for the reduced number density case and the corresponding baseline run (both with $v_d/v_{Ae} = 1.50$). The initial peak and decay phases are similar to Figure 2 (a-b) with features such as the initial filament and subsequent oblique whistler mode, and therefore we omit those times here for simplicity. For the case with equal number densities carrying the heat flux and return current in Fig. 7(a), the filament structure from the Weibel instability forms at the bottom of the domain and extends upward, threading the entire system. In Fig. 7(b), where the number density of electrons carrying the heat flux is reduced, the Weibel instability is weaker and filaments only extend to the middle of the box before they are replaced by oblique whistler waves.

Shown in Fig. 8 is the time evolution of the box-averaged magnetic fluctuation energy $\langle B_z^2 \rangle$ for the base case with $v_d/v_{Ae} = 1.50$ and the case with reduced number density carrying the heat flux (corresponding to the red point in Fig. 3 and Fig. 7 panel (b)). When the initial heat flux is reduced by half (with the same drift speed), the wave energy before $t\Omega_e = 400$ is small due to the reduced population of electrons available to drive the instability. Eventually the slowly growing waves reach finite amplitude and the fluctuation level flattens around $t\Omega_e = 800$. The late time value of the wave amplitude is only modestly reduced from that of the base case, demonstrating that strong oblique whistler waves can be excited even when the number density of the electrons carrying the heat flux is reduced.
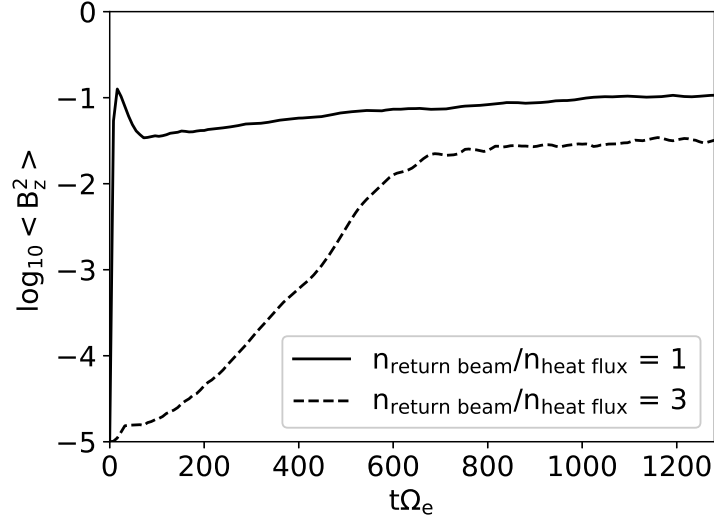
Figure 8. Box-averaged out-of-plane magnetic fluctuation amplitude B_z^2 as a function of time for the simulation with the reduced number density of electrons carrying the heat flux (dashed curve) and the corresponding base case (solid curve). Both have $v_d/v_{Ae} = 1.50$.
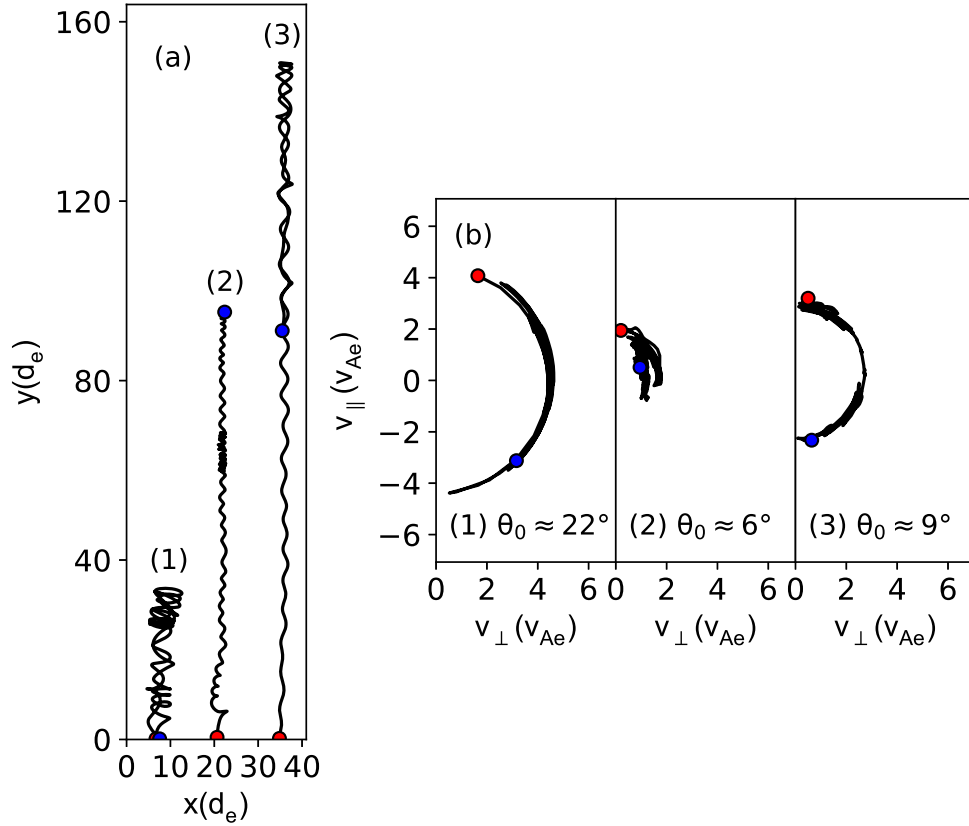

Figure 9. (a) Electron trajectories in the $x - y$ plane for the strong drift case with $v_d/v_{Ae} = 2.12$. Three electron trajectories are shown with red dots indicating the starting positions and blue dots the end positions. The trajectories are from the middle of the simulation (around $t\Omega_e = 900$). (b) Electron velocity trajectories correspond to the three cases in panel (a) in $v_\parallel - v_\perp$ space. Red dots indicate the starting positions and blue dots are the end of the trajectories. θ_0 gives the initial pitch angle.

Shown in Fig. 9 are the self-consistent trajectories of several electrons in the $x - y$ and $v_\parallel - v_\perp$ planes, extracted from the particle-in-cell simulation with $v_d/v_{Ae} = 1.50$. The electrons all start from the bottom boundary with initial parallel velocities significantly greater than their perpendicular velocities and so are typical of electrons carrying the heat flux. In panel (a), the waves in the system are strong enough to completely reverse the direction of the electrons (they are scattered past 90° in pitch angle). In panel (b), the trajectories of case (1) and (3) exhibit diffusion along a nearly complete semi-circle (see Eq. (2)) and scatter over 90 degrees in pitch angle, reversing their direction along the ambient magnetic field. The particle in case (2) also scatters past 90 degrees but reveals a more complex trajectory as it moves from a larger to a smaller radius in velocity space. The trajectories demonstrate that the reduction of electron parallel velocity is accompanied by an increase of perpendicular velocity. Thus, the scattering of whistler waves has significant consequences: it directly inhibits the heat flux while at the same time boosting the potential for magnetic trapping by increasing the pitch angle. Both effects will boost the confinement of energetic electrons in flares.

We now compute the wave-particle scattering rate that leads to the reduction in electron anisotropy and examine its scaling with parameters. There is no single such formalism for determining the rate because of the nonlinear nature of different scattering processes (e.g., weak scattering as described by quasilinear theory versus trapping in finite amplitude waves) (Gary et al. 2000). For example, Hamasaki & Krall (1973) used quasilinear theory to determine the scattering rate of the whistler anisotropy instability while others have approximated the scattering due to the proton cyclotron instability by finding the maximum exponential decay rate of the temperature anisotropy (Gary et al. 2000; Nishimura et al. 2002). Here is we use the Lorenz scattering operator, which describes electrons scattering off a stationary center, to model the relaxation of the temperature anisotropy in the simulations and to deduce the scattering rate. The Lorenz operator is give by

$$\left(\frac{\partial f_e}{\partial t}\right)_e = \frac{\nu_e}{2}\frac{\partial}{\partial \xi}\left(1 - \xi^2\right)\frac{\partial}{\partial \xi}f_e \tag{9}$$

where $\xi = \cos\theta$ and ν_e is the electron scattering rate. By taking moments of this equation to determine the rate of relaxation of the temperature anisotropy of the electron velocity distribution, we obtain a formula for ν_e,

$$\nu_e = \frac{dR/dt}{2 - R - R^2} \tag{10}$$

where $R = T_\parallel/T_\perp$ is the temperature anisotropy of the total electron distribution. We use this equation to model the relaxation of the temperature anisotropy near the low boundary of the simulation domain that is shown at late time in Fig. 2. The anisotropy profile has reached a steady state so the total time derivative in Eq. (10) reduces to the convective derivative

$$\nu_e = v_y \frac{\partial R/\partial y}{2 - R - R^2}, \tag{11}$$

where v_y is a constant equal to the heat flux drift speed at the lower boundary. The temperature anisotropy curves in Fig. 2 were smoothed with a Gaussian filter and the calculated scattering rates were averaged over the ranges of $0 \lesssim y \lesssim 80d_e, 0 \lesssim y \lesssim 60d_e, 0 \lesssim y \lesssim 10d_e, 0 \lesssim y \lesssim 4d_e$, for the cases of drift speed $v_d/v_{Ae} = 0.75, 1.06, 1.50,$ and 2.12, respectively. In Fig. 10 we plot the wave-particle scattering rate for electron anisotropy reduction from the four simulations (Fig. 1). For the weakest drift case $v_d/v_{Ae} = 0.75$, the scattering rate is very small $\left(\sim 10^{-4}\Omega_e\right)$, while for larger drift cases the scattering rates are significantly larger, growing to $\sim 6 \times 10^{-2}\Omega_e$. The figure reveals that the scattering rate scales as a linear function of v_d/v_{Ae}, the ratio of the drift speed to electron Alfvén speed, above a threshold given by $v_d/v_{Ae} \sim 1$.

4. CONCLUSIONS

Observations and theory imply that there is suppression of the transport of energetic electrons during solar flares. We have explored pitch-angle scattering by oblique whistler waves and Weibel-driven disturbances as a mechanism for reducing the electron heat flux. The energetic electron heat flux escaping from a flare-like system excites strong oblique whistler waves through the anomalous cyclotron resonance. These waves pitch-angle scatter the electrons on a rapid timescale of hundreds of electron cyclotron periods, suppressing the heat flux and increasing the perpendicular velocities of electrons. At high mean drift speeds compared with v_{Ae} the nonthermal electrons can also drive the Weibel instability. The resulting scattering mechanisms can operate under the generic conditions of reconnection-driven electron energization and can reduce the field-aligned electron energy flux by up to a factor of two. Of greater
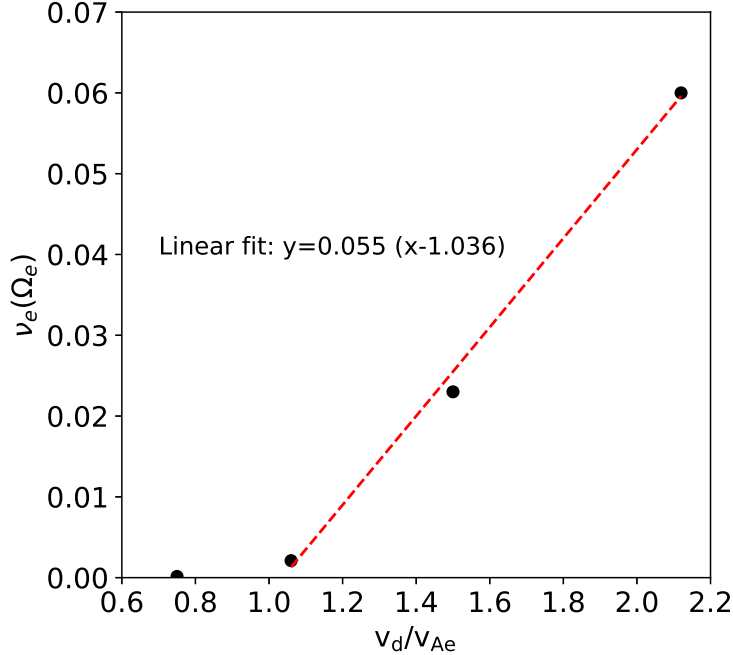
Figure 10. The averaged wave-electron scattering rate at late time for the four runs in Fig. 1 as a function of v_d/v_{Ae}, the ratio of mean parallel drift speed of heat flux to electron Alfvén speed. The scattering rate is calculated from Eq. (11) and is averaged over the ranges of $0 \lesssim y \lesssim 80d_e, 0 \lesssim y \lesssim 60d_e, 0 \lesssim y \lesssim 10d_e, 0 \lesssim y \lesssim 4d_e$ for the drift speeds $v_d/v_{Ae} = 0.75, 1.06, 1.50,$ and 2.12, respectively. The red dashed line shows a linear fit to the data above the threshold $v_d/v_{Ae} \approx 1$.

significance is that this scattering process increases the energetic electrons' perpendicular velocity so that the electrons will more effectively mirror and can be trapped in the large-scale magnetic fields of the flare energy release region. This scattering mechanism can therefore suppress the escape of electrons from the energy release regions of flares, which is required for them to reach the relativistic velocities documented in observations.

In previous simulations treating whistler waves in flares, the fluctuations damp out after scattering is complete and the heat flux from the initial electron distribution is reduced (Roberg-Clark et al. 2019). In contrast, in the current simulations the oblique whistler waves and Weibel perturbations are maintained in a steady-state due to the continual injection of heat flux from the boundary. This mimics the continued energy release from reconnection during flares. Such a setup represents a more physically reasonable set of initial conditions and avoids the influence of arbitrary discontinuities in the initial distribution function, giving more confidence to the interpretation of the final results. We suggest, on the basis of the present simulations, that oblique whistler waves and Weibel disturbances can grow to large amplitude during flares and scatter electrons to reduce their heat flux.

Although our model was designed to study the transport of energetic electrons in flares, the model is relevant to any $\beta \sim 1$, weakly collisional plasmas with high heat flux due to the presence of nonthermal electrons. Astrophysical applications might include accretion disc coronae (Bisnovatyi-Kogan & Ruzmaikin 1976; Liang & Price 1977; Uzdensky & Goodman 2008). Scattering by oblique whistlers of the solar wind strahl into the halo population is currently under active investigation (Boldyrev & Horaites 2019; Verscharen et al. 2019; Vasko et al. 2019). Observations at 1AU have shown that the pitch angle widths of strahl in the presence of whistler mode waves are up to 12° larger than that in the absence of whistler waves (Kajdič et al. 2016). Large-amplitude, oblique whistlers that would limit the electron heat flux have been detected in the solar wind (Breneman et al. 2010; Cattell et al. 2020), in the magnetosphere (Kellogg et al. 2011), and in flares (Huang et al. 2016). Simulations show that oblique whistler waves excited by the strahl component under solar wind conditions can scatter the strahl distribution into the halo and reduce the strahl-carried heat flux (Vo 2021; López et al. 2019; Micera et al. 2020). Our simulations are focused on the flare system, where the electron heat flux is much greater than in the case of the solar wind strahl. Nevertheless, our model clarifies the mechanism for scattering of energetic electrons by whistlers that is also active in the strahl scattering problem.

We note that our results may be limited by the common disadvantages of particle-in-cell simulations such as small domains and short timescales compared with those of real flares. On the other hand, the scale size of turbulence associated with whistlers and the Weibel instability is at the kinetic scale so the typical scale separation issue is less of a problem than in the exploration of electron energy gain during magnetic reconnection. The initial electron velocity distribution contains an artificially sharp gradient near $v_y = 0$, but this gradient is transient in the system's evolution and its influence disappears by the time the system reaches a steady state. Further investigation is required to elucidate the transition mechanism from the Weibel instability to oblique whistler wave. Additionally, it is worth noting that magnetic field inhomogeneities resulting from turbulence or inherent mirror structure may affect transport suppression. The confinement of energetic electrons seems to result from a combination of magnetic trapping and wave scattering, so the exploration of particle scattering in a mirror geometry should be pursued in future studies.

REFERENCES

Allen, B., Yakimenko, V., Babzien, M., et al. 2012, Physical review letters, 109, 185007

Arnold, H., Drake, J. F., Swisdak, M., et al. 2021, Physical review letters, 126, 135101

Aschwanden, M. J., Caspi, A., Cohen, C. M., et al. 2017, The Astrophysical Journal, 836, 17

Bian, N., Emslie, A. G., Horne, D., & Kontar, E. P. 2018, The Astrophysical Journal, 852, 127

Bisnovatyi-Kogan, G., & Ruzmaikin, A. 1976, Astrophysics and Space Science, 42, 401

Boldyrev, S., & Horaites, K. 2019, Monthly Notices of the Royal Astronomical Society, 489, 3412

Breneman, A., Cattell, C., Schreiner, S., et al. 2010, Journal of Geophysical Research: Space Physics, 115

Cattell, C., Short, B., Breneman, A., & Grul, P. 2020, The Astrophysical Journal, 897, 126

Dahlin, J., Drake, J., & Swisdak, M. 2014, Physics of Plasmas, 21, 092304

—. 2016, Physics of Plasmas, 23, 120704

—. 2017, Physics of Plasmas, 24, 092110

Drake, J., Swisdak, M., Che, H., & Shay, M. 2006, Nature, 443, 553

Emslie, A., Kucharek, H., Dennis, B., et al. 2004, Journal of Geophysical Research: Space Physics, 109

Fleishman, G. D., Gary, D. E., Chen, B., et al. 2020, Science, 367, 278

Fleishman, G. D., Nita, G. M., Chen, B., Yu, S., & Gary, D. E. 2022, Nature, 1

Fonseca, R. A., Silva, L. O., Tonge, J. W., Mori, W. B., & Dawson, J. M. 2003, Physics of Plasmas, 10, 1979

Gary, D. E., Chen, B., Dennis, B. R., et al. 2018, The Astrophysical Journal, 863, 83

Gary, S. P., Yin, L., & Winske, D. 2000, Geophysical research letters, 27, 2457

Glesener, L., Krucker, S., Duncan, J., et al. 2020, The Astrophysical Journal Letters, 891, L34

Graham, G., Rae, I., Owen, C., et al. 2017, Journal of Geophysical Research: Space Physics, 122, 3858

Guo, J., Emslie, A. G., Massone, A. M., & Piana, M. 2012, The Astrophysical Journal, 755, 32

Hamasaki, S., & Krall, N. 1973, The Physics of Fluids, 16, 145

Hesse, M., & Cassak, P. 2020, Journal of Geophysical Research: Space Physics, 125, e2018JA025935

Huang, S., Fu, H., Yuan, Z., et al. 2016, Journal of Geophysical Research: Space Physics, 121, 6639

Huntington, C., Fiuza, F., Ross, J., et al. 2015, Nature Physics, 11, 173

Kadomtsev, B., & Pogutse, O. 1968, Sov. Phys. JETP, 26, 1146

Kajdič, P., Alexandrova, O., Maksimovic, M., Lacombe, C., & Fazakerley, A. 2016, The Astrophysical Journal, 833, 172

Karimabadi, H., Krauss-Varban, D., & Terasawa, T. 1992, Journal of Geophysical Research: Space Physics, 97, 13853

Kellogg, P., Cattell, C., Goetz, K., Monson, S., & Wilson III, L. 2011, Journal of Geophysical Research: Space Physics, 116

Komarov, S., Schekochihin, A., Churazov, E., & Spitkovsky, A. 2018, Journal of Plasma Physics, 84

Krall, N. A., & Trivelpiece, A. W. 1973, American Journal of Physics, 41, 1380

Krucker, S., Hudson, H., Glesener, L., et al. 2010a, The Astrophysical Journal, 714, 1108

Krucker, S., Hudson, H. S., Glesener, L., et al. 2010b, The Astrophysical Journal, 714, 1108, doi: 10.1088/0004-637X/714/2/1108

Krucker, S., White, S. M., & Lin, R. P. 2007, The Astrophysical Journal, 669, L49, doi: 10.1086/523759

Krucker, S., Battaglia, M., Cargill, P., et al. 2008, The Astronomy and Astrophysics Review, 16, 155

Levinson, A., & Eichler, D. 1992, The Astrophysical Journal, 387, 212

Li, T., Drake, J., & Swisdak, M. 2012, The Astrophysical Journal, 757, 20

—. 2014, The Astrophysical Journal, 793, 7

Li, T. C., Drake, J. F., & Swisdak, M. 2013, The Astrophysical Journal, 778, 144

Liang, E., & Price, R. H. 1977, The Astrophysical Journal, 218, 247

Lin, R. P., Krucker, S., Hurford, G. J., et al. 2003, The Astrophysical Journal, 595, L69, doi: 10.1086/378932

López, R., Shaaban, S., Lazar, M., et al. 2019, The Astrophysical Journal Letters, 882, L8

Maksimovic, M., Zouganelis, I., Chaufray, J.-Y., et al. 2005, Journal of Geophysical Research: Space Physics, 110

Masuda, S., Kosugi, T., Hara, H., Tsuneta, S., & Ogawara, Y. 1994, Nature, 371, 495

Micera, A., Zhukov, A., Lopez, R. A., et al. 2020, in APS Division of Plasma Physics Meeting Abstracts, Vol. 2020, TO16–010

Moore, R., McKenzie, D., Svestka, Z., et al. 1980, in Skylab Solar Workshop II, 341–409

Morse, R., & Nielson, C. 1971, The Physics of Fluids, 14, 830

Nishimura, K., Gary, S. P., & Li, H. 2002, Journal of Geophysical Research: Space Physics, 107, SMP

Oka, M., Ishikawa, S., Saint-Hilaire, P., Krucker, S., & Lin, R. 2013, The Astrophysical Journal, 764, 6

Parail, V., & Pogutse, O. 1978, Nuclear Fusion, 18, 303

Petrosian, V., Donaghy, T. Q., & McTiernan, J. M. 2002, The Astrophysical Journal, 569, 459

Roberg-Clark, G., Agapitov, O., Drake, J. F., & Swisdak, M. 2019, The Astrophysical Journal, 887, 190

Roberg-Clark, G., Drake, J., Reynolds, C., & Swisdak, M. 2018a, Physical Review Letters, 120, 035101

Roberg-Clark, G., Drake, J. F., Swisdak, M., & Reynolds, C. 2018b, The Astrophysical Journal, 867, 154

Roberg-Clark, G. T., Drake, J., Reynolds, C., & Swisdak, M. 2016, The Astrophysical Journal Letters, 830, L9

Simões, P. J., & Kontar, E. P. 2013, Astronomy & Astrophysics, 551, A135

Spitzer, L. 2006, Physics of fully ionized gases (Courier Corporation)

Stix, T. 1992, and, 26, 6

Štverák, Š., Maksimovic, M., Trávníček, P. M., et al. 2009, Journal of Geophysical Research: Space Physics, 114

Uzdensky, D. A., & Goodman, J. 2008, The Astrophysical Journal, 682, 608

Vasko, I., Krasnoselskikh, V., Tong, Y., et al. 2019, The Astrophysical Journal Letters, 871, L29

Verscharen, D., Chandran, B. D., Jeong, S.-Y., et al. 2019, The Astrophysical Journal, 886, 136

Vo, T. 2021, arXiv preprint arXiv:2105.02265

Vo, T., Lysak, R., & Cattell, C. 2022, Physics of Plasmas, 29, 012904

Warmuth, A., & Mann, G. 2016, Astronomy & Astrophysics, 588, A115

Weibel, E. S. 1959, Physical Review Letters, 2, 83

Weihan, T., & Min, G. 1985, Laser and Particle Beams, 3, 243

Yamada, M., Kulsrud, R., & Ji, H. 2010, Reviews of modern physics, 82, 603

Yoon, P. H. 2007, Physics of Plasmas, 14, 024504

Yoon, P. H., & Davidson, R. C. 1987, Physical Review A, 35, 2718

Zeiler, A., Biskamp, D., Drake, J., et al. 2002, Journal of Geophysical Research: Space Physics, 107, SMP